Nano Energy 64 (2019) 103930

Contents lists available at ScienceDirect

Nano Energy

journal homepage: www.elsevier.com/locate/nanoen

Full paper

< 50-μm thin crystalline silicon heterojunction solar cells with dopant-free carrier-selective contacts

Hao Dai[a], Liu Yang[a,b,*], Sailing He[a,b,c,**]

[a] Center for Optical and Electromagnetic Research, National Engineering Research Center for Optical Instrumentation, Zhejiang University, Hangzhou, 310058, China
[b] Ningbo Research Institute, Zhejiang University, Ningbo, 315100, China
[c] JORCEP, School of Electrical Engineering, Royal Institute of Technology (KTH), S-100 44, Stockholm, Sweden

ARTICLE INFO

Keywords:
Crystalline silicon heterojunction solar cell
Dopant-free carrier-selective contacts
Thin wafer
Passivation
Band bending

ABSTRACT

Dopant-free carrier-selective contacts are emerging in the field of crystalline silicon (c-Si) photovoltaic solar cells, which are potential to further improve the power conversion efficiency (PCE) and lower the cost of c-Si solar cells. Here, we demonstrate tens of microns thin c-Si heterojunction solar cells with substochiometric MoO_x and LiF_x as dopant-free hole- and electron-selective contacts, respectively. Chemical thinning of 200-μm thick c-Si wafers enables the production of proof of concept devices with good flexibility and strong performance. When the wafer thickness is reduced to 49.4 μm (24.7% of the initial thickness), the power conversion efficiency (PCE) of the solar cell still maintains 88.2% of the initial value for the 200-μm thick cell. When the wafer thickness becomes less than 10% (or even 3.4%) of the initial value, 61.2% and 39.2% of the initial PCEs are still achieved for the 14.8- and 6.8-μm thick cells, respectively. Passivating and carrier-selective effects of the MoO_x and LiF_x films allow for the maintenance of performance. An oxide interlayer at the MoO_x/c-Si interface passivates the dangling bonds of the c-Si surface and improves the minority carrier lifetime. Field-effect passivation and carrier-selective effects induced by the band bending near the MoO_x/c-Si interface and the Al/LiF_x/c-Si interface play an important role in maintaining high open-circuit voltage and high fill factor. To the best of our knowledge, this is the first time that < 100-μm thin c-Si heterojunction solar cells are reported with undoped contacts. Our solar cells have been fabricated on thin c-Si wafers with low-temperature processes and without additional doping, and thus our work provides a promising cost-effective means in the field of thin and flexible c-Si solar cells.

1. Introduction

Crystalline silicon (c-Si) solar cells are one of the most prominent and mature photovoltaic technologies with broad implementation across many markets. The power conversion efficiency (PCE) reached 25.0% in 1999 [1,2], and has moved up slightly to 25.6% in 2014 [3] and to 26.7% in 2017 [4,5], approaching the theoretical limit [6]. In order to further improve the PCE and lower the cost, traditional c-Si solar cells have to be optimized substantially. c-Si photovoltaics are typically based on heavily-doped carrier-selective contacts, forming homojunctions or heterojunctions for separating and extracting photogenerated carriers. The homojunctions use boron- or aluminum-diffused p^+-type hole-selective contacts and phosphorus-diffused n^+-type electron-selective contacts [1,2], while the heterojunctions employ p^+-type and n^+-type heavily-doped hydrogenated amorphous silicon (a-Si:H) respectively as hole- and electron-selective contacts (with intrinsic a-Si:H as passivation coatings on the c-Si surfaces) [3,4]. Despite the achievements in pushing PCE to over 25% [1–5], these heavy doping technologies still have many shortcomings, which limit the cost and device performance. Heavily-doped semiconductors exhibit significant Auger recombination, bandgap narrowing, bulk/surface recombination, free-carrier absorption, etc [7–11]. All these unfavorable factors will greatly limit the open-circuit voltage and the short-circuit current of the solar cells, affecting the cell PCEs. High-temperature diffusion and annealing processes are always necessary for doping. Toxic and flammable gases (i.e., borane and phosphine) are required for the growth of p^+-type and n^+-type a-Si:H. The doping processes are complex, meaning costly and relatively unfriendly to the environment.

In recent years, dopant-free carrier-selective contacts have been proposed [12,13], where hetero-contacts are formed on c-Si using

* Corresponding author. Center for Optical and Electromagnetic Research, National Engineering Research Center for Optical Instrumentation, Zhejiang University, Hangzhou, 310058, China.
** Corresponding author. Center for Optical and Electromagnetic Research, National Engineering Research Center for Optical Instrumentation, Zhejiang University, Hangzhou, 310058, China.
E-mail addresses: optyang@zju.edu.cn (L. Yang), sailing@zju.edu.cn (S. He).

https://doi.org/10.1016/j.nanoen.2019.103930
Received 26 May 2019; Received in revised form 21 July 2019; Accepted 23 July 2019
Available online 24 July 2019

materials with different workfunctions to selectively extract photogenerated carriers from c-Si. Without additional doping, the above-mentioned physical and technological issues can be avoided. Such c-Si solar cells show great potential to further improve the PCE and reduce the cost, therefore quickly becoming a new hot topic in the field of c-Si solar photovoltaics. Many recent reports explore dopant-free materials for conduction of electrons and holes from c-Si, respectively. Low-workfunction metals, such as calcium (Ca; ~2.9 eV) [14] and magnesium (Mg; 3.7 eV) [15], have been proposed to form electron-selective contacts with n-type c-Si. The metal/c-Si interfaces can be passivated by substoichiometric TiO_x [16–18], MgO_x [19], SiO_x [20] or barrier-lowering materials, such as substoichiometric LiF_x [21] and MgF_x [22]. Inserting Ca between aluminum (Al) and TiO_x could lower the Al/TiO_x contact resistance by about 2 orders of magnitude for electron conduction and the cell PCE was greatly enhanced [23]. For hole conduction, high-workfunction materials are favorable. Substoichiometric transition metal oxides, such as MoO_x [24–29], WO_x [28–30], and V_2O_x [29], which are widely employed in organic optoelectronics [31], have recently been introduced into c-Si solar cells. These materials represent a significant improvement over the doped hole-selective contacts. In comparison with p-type organic hole-selective materials (e.g., PEDOT:PSS and Spiro-OMeTAD) [32–34], these inorganic materials are much more stable. With dopant-free contacts for both electron and hole extraction, Bullock et al. reported an efficient c-Si solar cell with PCE of 19.4%, where LiF_x and MoO_x were employed as the electron- and hole-selective contacts, respectively and the c-Si surfaces were passivated with intrinsic a-Si:H [35]. Without the passivation layer, Um et al. reported an all-back-contact c-Si solar cell with PCE of 15.4% [36]. Though the reported PCEs were lower than those of traditional c-Si solar cells with doped contacts [35,36], the effectiveness of the dopant-free contacts for high-efficiency c-Si solar cells has been demonstrated.

The c-Si solar cells mentioned above are all based on thick c-Si wafers with thicknesses over 100 μm (most over 200 μm) [1–4,14–30,35,36]. Besides the drawback of higher cost, thicker c-Si wafers have stronger bulk recombination, which leads to stricter quality requirements for the wafers. Using thinner c-Si reduces the cost of solar cell, and potentially improves the open-circuit voltage due to the reduction of the bulk recombination [37]. The wafer becomes increasingly light and flexible when the thickness is reduced [38], enabling some additional applications of c-Si solar cells that require light weight and strong mechanical flexibility. Several different thin c-Si solar cells have been reported, such as, 43-μm [39] and 10-μm [40,41] thick homojunction c-Si solar cells, 20-μm thick organic-inorganic hybrid c-Si solar cells [42], etc. All these thin c-Si solar cells have doped contacts [39–42] and inevitably suffer from the physical and technological issues induced by heavy doping as mentioned above. As far as we know, there have been no reports on dopant-free carrier-selective contacts for c-Si solar cells with thicknesses less than 100 μm.

Here we report the fabrication and characterization of c-Si solar cells with undoped contacts based on thin wafers of thicknesses between 50 μm and 6.8 μm. MoO_x and LiF_x serve as the dopant-free carrier-selective contacts. The PCE decreases with the reduction of wafer thickness, but the PCE degradations are much smaller than the thickness reductions, showing that very good power conversion can be maintained for < 50-μm thin c-Si solar cells. Sub-10 μm thin solar cells are much lighter and more flexible than thicker cells, and therefore are more suitable for portable and wearable power sources. From the scientific point of view, it is challenging to fabricate sub-10 μm thin c-Si solar cells because the wafers are very brittle. The success in device fabrication can help with the understanding of the performances of ultrathin c-Si solar cells and the potential of sub-10 μm c-Si wafers for optoelectronic devices. It will provide a guide for the development of the emerging flexible optoelectronics.

2. Experimental Section

2.1. Wafer thinning and device fabrication

200-μm thick n-type (100) float-zone double-side polished c-Si wafers (resistivity: 1–5 Ω·cm) were employed to fabricate thin c-Si heterojunction solar cells with thicknesses below 50 μm. Before thickness reduction and device fabrication, the wafers were thoroughly cleaned as follows: First, the wafers were ultrasonically cleaned in a sequence of acetone, isopropanol, and then deionized (DI) water each for 10 min. Then, they were immersed into an ammonia ($NH_3{\cdot}H_2O$) and hydrogen peroxide (H_2O_2) solution ($NH_3{\cdot}H_2O{:}H_2O_2$ = 1:1 by weight) for 10 min, followed by a 20-min immersion in piranha solution ($H_2SO_4{:}H_2O_2$ = 4:1 by weight). After each step, the wafers were rinsed with DI water and dried by nitrogen.

To reduce the wafer thickness, the clean c-Si wafers were etched in a 50 wt% potassium hydroxide (KOH) solution at 90 °C. Thin wafers with different thicknesses could be obtained by varying the etching time. Then, the thin wafers were soaked into a dilute hydrochloric acid (HCl) and H_2O_2 solution ($HCl{:}H_2O_2{:}H_2O$ = 1:1:5 by weight) for 2–3 h, in order to remove the silicate and orthosilicic acid produced in the etching procedure.

Before device fabrication, the thin wafers were cleaned again with the above procedures and then immersed in a dilute 4 wt% hydrofluoric (HF) acid aqueous solution for about 2 min to remove the silicon dioxide (SiO_2) layer produced during the cleaning procedures. Together with the chemical removal of the residuals produced in the etching procedure, the wafers experienced multiple cleanings with different solutions after being etched. This guaranteed a relatively small roughness of the c-Si surfaces for the following device fabrication (to be demonstrated below). Immediately after being dried in an oven at 90 °C for 10 min, the c-Si thin wafers were transferred to a thermal evaporator (VNANO VZZ-300S) for the deposition of dopant-free carrier-selective contact materials as well as top and bottom electrodes. On the rear side of the wafer, to selectively collect photogenerated electrons, a ~2-nm thick substoichiometric $LiF_{x\ (x<1)}$ film as well as a ~100-nm thick aluminum (Al) film were evaporated in sequence without breaking the vacuum condition. On the front side, to selectively collect photogenerated holes, a ~23-nm thick substoichiometric $MoO_{x\ (x<3)}$ film was deposited followed by a deposition of a ~100-nm thick silver (Ag) grid electrode with a shadow mask. The Ag gride thickness was in consistence with that reported in Ref. [24], and was thick enough for conduction (to be shown below). Unlike most MoO_x-based hole-selective contacts reported previously [24,25,27–29,35], here in this work, no transparent conductive oxide (TCO) layer, such as indium tin oxide and hydrogenated indium oxide, was applied between the MoO_x film and the Ag grid electrode. Without the protection of the TCO film, the performances of our cells might degrade upon air exposure because of the sensitivity of MoO_x to adventitious carbon and water adsorption [24]. We note that those TCOs are usually deposited by sputtering in a pure argon plasma environment [24,25,27–29,35]. The bombardment with energetic particles can introduce increased oxygen vacancies, and the plasma UV luminescence can cause photochromism of MoO_x [43], both leading to increased parasitic absorption in the MoO_x film [27]. An interlayer between MoO_x and TCO has been observed, which affected negatively the hole collection efficiency [27]. Also considering the fragility of those TCOs, we did not incorporate any TCOs in our thin flexible c-Si solar cells. In our future work, alternative flexible transparent conductive electrodes to TCOs, such as Ag nanowires networks developed in our group [44,45], will be studied and incorporated into our thin flexible solar cells. Since the thin c-Si wafers, especially those with thicknesses less than 10 μm, were very fragile and easy to crack, during the whole process, the wafers were very carefully handled without any additional substrates. Shear force were avoided. Small DI water flow was applied to clean the wafers and weak nitrogen flow was allowed to dry the wafers. For comparison, such solar cells were also

fabricated on the original 200-μm thick c-Si wafers with the above procedures excluding the wafer thinning step. In the whole procedure, no doping nor temperature above 90 °C were necessary.

2.2. Characterizations

Cross-sections of the c-Si thin wafers were observed using scanning electron microscopy (SEM; Carl Zeiss Ultra 55). The wafer surfaces developed around 20 nm of surface roughness after KOH etching, which could be characterized using atomic force microscopy (AFM; Being CSPM 5500). A home-built integrating sphere spectrometer was employed to measure the reflection and transmission spectra of the thin wafers, through which the absorption spectra could be easily calculated. Minority carrier lifetime was measured with a quasi-steady-state photoconductance decay tester (Sinton WCT-120). The Al/LiF_x/c-Si and MoO_x/c-Si interfaces were observed with a field-emission transmission electron microscope (TEM; FEI Tecnai G2 F20 S-TWIN) and the TEM sample was fabricated by focused ion beam milling (Carl Zeiss Quata 3D FEG). Distributions of Mo, O, and Si along the depths from MoO_x to c-Si were detected using energy-dispersive spectroscopy (EDS) on the TEM. To characterize the substoichiometry of MoO_x, X-ray photoelectron spectroscopy (XPS) analysis was conducted with a VG ESCALAB MARK II system. For the characterization of the fabricated solar cells, the current density-voltage (J-V) curves were measured by a source meter (Keithley 2450) under 1-sun illumination from a solar simulator (SAN-EI ELECTRIC AAA). Characteristic parameters including the short-circuit current density (J_{sc}), open-circuit voltage (V_{oc}), fill factor (*FF*) as well as the PCE (η) were extracted from the J-V curve. Series and shunt resistances were also calculated through the slopes of the J-V curve at the points of V_{oc} and J_{sc}, respectively. External quantum efficiencies (EQEs) of our solar cells were measured with an EQE tester (PV Measurements QEX10).

3. Results and discussions

3.1. Flexible c-Si wafers with thicknesses less than 50 μm

Through chemical etching, 200-μm thick c-Si wafers could be reduced to different thicknesses (t_{Si}) for different etching times. SEM characterization (Fig. 1(a) and (b)) confirmed that ultrathin c-Si films were successfully fabricated with thicknesses of 6.8 and 14.8 μm, respectively. c-Si wafers with t_{Si} > 100 μm are brittle and could not be bent, while with reduced thickness the device can become flexible. In Fig. 1(c–e), three < 50-μm thick c-Si wafers all demonstrated very good flexibility. The thinnest wafer with t_{Si} = 6.8 μm could easily be bent into a circle with radius as small as 1.5 mm (Fig. 1(c)); while the other two thicker samples with t_{Si} = 14.8 and 49.4 μm could only be bent into semicircles with bending radii of 3.5 and 6.5 mm, respectively (Fig. 1(d) and (e)).

Absorption (Fig. 2(a)), reflection (Fig. 2(b)) as well as transmission (Fig. 2(c)) spectra of the c-Si thin wafers showed similar optical performance of all films in the most of the visible region. In the near-infrared regime, thinner wafers introduced stronger reflectance due to the reflection at the bottom c-Si surface and also stronger transmittance (red light transmission was observed when the 6.8-μm thick c-Si film was illuminated by a white light, as shown in the inset of Fig. 2(c)). Consequently, degradation of absorption was observed, which was greater as the wafer became thinner (Fig. 2(a)). Fortunately, the absorption spectra were almost the same over the main peak of the solar spectrum, and the etched c-Si wafers with reduced thicknesses (t_{Si} < 50 μm) even demonstrated a little bit higher absorption in this range.

After thickness reduction through KOH etching, the surface roughness of the c-Si wafer increased from 0.4 nm (Fig. 2(d)) to 18.7 nm (Fig. 2(e)). This roughness was relatively smaller than what was expected from the very fast KOH etching process. Short-wavelength photons incident on such rough surface would be scattered, which might be the reason behind the slightly enhanced absorption in Fig. 2(a). Such morphological changes indeed affected minority carrier lifetime adversely due to the increased surface area and thus surface traps (Fig. 2(f)). The lifetime was also negatively affected by the electron-selective contact material (LiF_x). But fortunately, when the hole-selective contact material (MoO_x), was deposited on top of the surfaces, minority carrier lifetime increased for both original and etched c-Si wafers as discussed later.

3.2. Thin c-Si heterojunction solar cells based on dopant-free carrier-selective contacts

Based on the thinned c-Si wafers, thin c-Si heterojunction solar cells based on dopant-free carrier-selective contacts were fabricated, as schematically shown in Fig. 3(a). Ag/MoO_x and Al/LiF_x were deposited on the front and rear side of the c-Si wafer to form heterojunctions to the c-Si. The substoichiometric high-workfunction MoO_x and low-workfunction LiF_x on the two sides bend the energy band to allow the photogenerated holes (electrons) to be collected by the front Ag/MoO_x

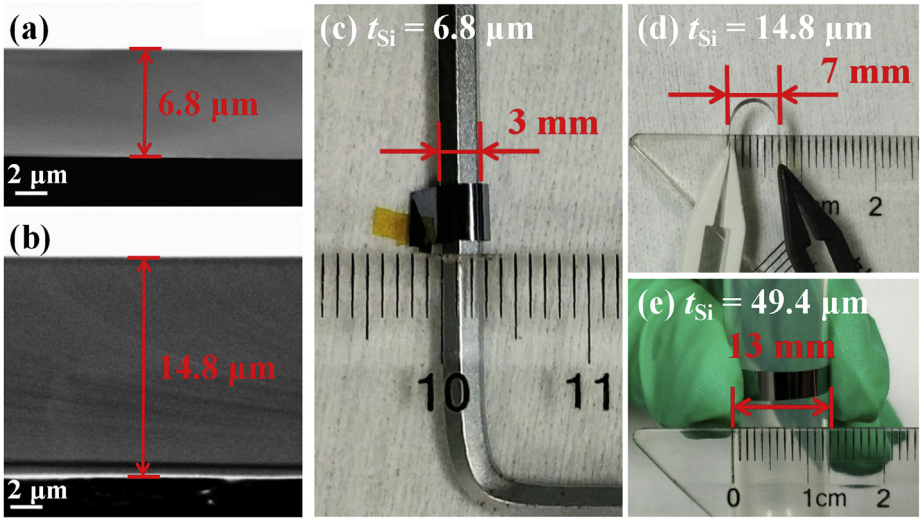

Fig. 1. Cross-sectional SEM images of c-Si thin wafers, indicating the wafer thicknesses (t_{Si}) of (a) 6.8 and (b) 14.8 μm, respectively; Photo pictures of bent c-Si wafers with t_{Si} = (c) 6.8, (d) 14.8, and (e) 49.4 μm, respectively.

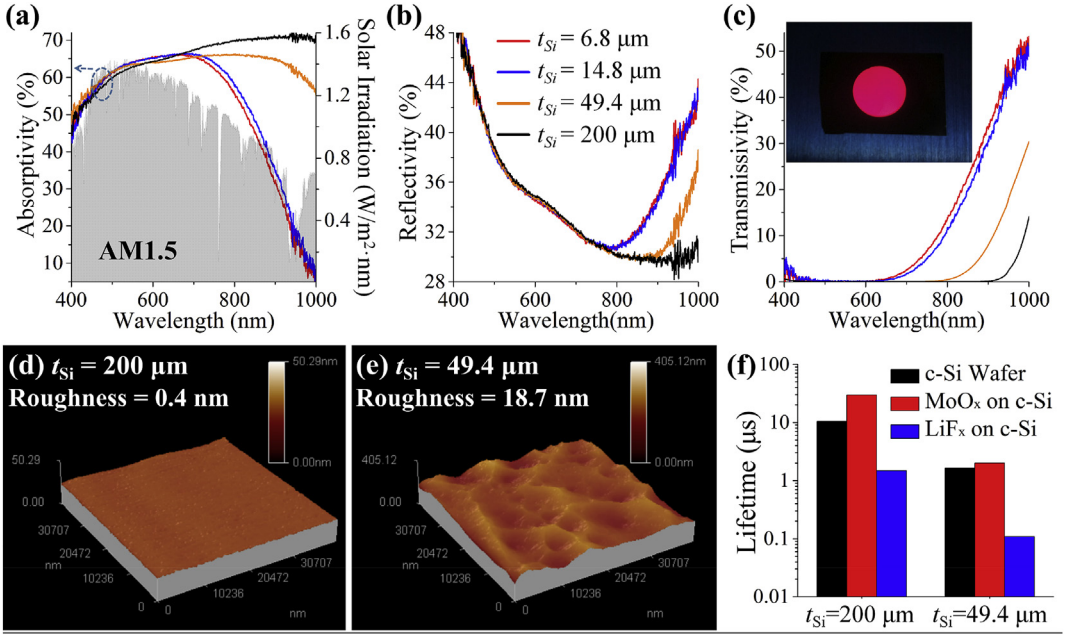

Fig. 2. (a) Absorption, (b) reflection, and (c) transmission spectra of c-Si wafers with thicknesses of t_{Si} = 6.8, 14.8, 49.4, and 200 μm. The inset of (c) shows a photo of red light transmission through the 6.8-μm thick c-Si wafer under white light illumination. Surface morphologies of (d) the original 200-μm thick c-Si wafer and (e) the etched 49.4-μm thick c-Si wafer. (f) The minority carrier lifetime of these c-Si wafers, and the lifetime after deposition of MoO_x and LiF_x layers on c-Si.

(rear Al/LiF_x) contact and the opposite electrons (holes) to be blocked. The equally important roles of the front and rear hetero-contacts were to be explained in detail in Section 3.3. The flexibility of the wafer is maintained in the finished device (Fig. 3(b)). Excluding the shadow area of the Ag grid, the effective illuminated area of the solar cell was ~23 mm^2, well within the dashed box defined by the main grid shown in Fig. 3(a). The fabrication and characterization details were described in the Experimental Section. To test the process repeatability, three c-Si heterojunction solar cells based on the 200-μm thick wafers were fabricated and characterized. The three J-V curves and the corresponding characteristic parameters (Fig. S1 and Table S1, Supporting Information) were nearly identical. In our solar cells, the ~23-nm thick MoO_x and ~2-nm thick LiF_x allowed for much better power conversion performances than either thinner MoO_x (e.g., ~10 nm) or thinner LiF_x (e.g., ~1 nm), as shown in Fig. S2 and Table S2, Supporting Information. This was mainly due to the fact that the absence of passivation needed to be compensated with thicker high-workfunction MoO_x and thicker low-workfunction LiF_x for efficient hole and electron extractions, respectively. Without additional antireflection layer (e.g., a TCO coating), the top MoO_x layer had also to become thicker to trap more

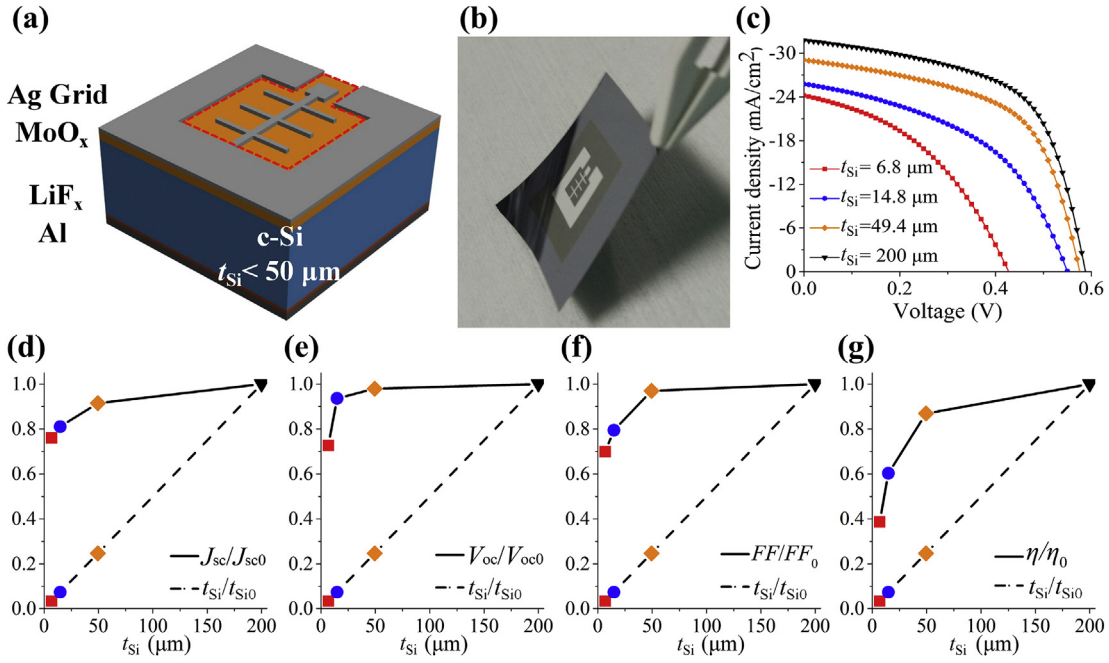

Fig. 3. Photovoltaic performances of our c-Si heterojunction solar cells based on dopant-free carrier-selective contacts with thickness t_{Si} = 6.8, 14.8, 49.4, and 200 μm: (a) Schematic diagram; (b) photo image of a bent c-Si solar cell with t_{Si} = 6.8 μm; (c) measured J-V curves; normalized characteristic parameters of (d) J_{sc}/J_{sc0}, (e) V_{oc}/V_{oc0}, (f) FF/FF_0, and (g) η/η_0 with respect to those with t_{Si} = 200 μm, in comparison with the normalized c-Si wafer thicknesses (t_{Si}/t_{Si0}).

Table 1
Characteristic parameters of c-Si heterojunction solar cells based on dopant-free carrier-selective contacts with different thicknesses.

t_{Si} (μm)	J_{sc} (mA/cm^2)	V_{oc} (mV)	FF (%)	η (%)	R_s (Ω·cm^2)	R_{sh} (Ω·cm^2)
6.8	24.19	427	41.032	4.24	7.06	57.99
14.8	25.76	550	46.615	6.61	5.61	100.19
49.4	29.08	576	56.910	9.53	3.26	109.89
200	31.64	587	58.187	10.819	3.16	134.45

light. Detailed comparisons could be found in Section S2, Supporting Information, while the inherent passivating and carrier-selective effects of both MoO_x and LiF_x were to be discussed in detail in Section 3.3 below.

Fig. 3(c) showed J-V curves of the fabricated c-Si heterojunction solar cells with t_{Si} = 6.8, 14.8 and 49.4 μm, respectively. The corresponding characteristic parameters were summarized in Table 1. For comparison, the averaged J-V curve and the corresponding characteristic parameters of the three 200-μm thick c-Si solar cells were also included in Fig. 3(c) and Table 1. The power conversion performances for the thin solar cells show the potential for thin devices to produce almost the same overall performance as much thicker devices at greatly reduced material usage. When the c-Si thickness decreased from 200 μm (η = 10.81%) to 49.4 μm (η = 9.53%), there was only 11.8% less performance. The 14.8-μm and the 6.8-μm thick c-Si solar cells were still functional with η = 6.61% and 4.24%, respectively.

In order to see the degradation of the characteristic parameters with the reduced c-Si thickness, normalized short-circuit current density (J_{sc}/J_{sc0}), open-circuit voltage (V_{oc}/V_{oc0}), fill factor (FF/FF_0), PCE (η/η_0) to those of the 200-μm thick c-Si solar cell were plotted respectively in Fig. 3(d)-3(g) as a function of the c-Si thickness. In each panel, the ratios of the c-Si film thickness to 200 μm were also plotted so as to compare the variation rates of the characteristic parameters. Due to the insufficient sunlight absorption induced by the reduced c-Si thickness, J_{sc} decreased as the c-Si thickness decreased. Fortunately, the J_{sc} degraded very slowly and only 23.9% of the degradation was observed when c-Si thickness (t_{Si}) was reduced by 96.9% from 200 μm to 6.8 μm (Fig. 3(d)). As shown in Fig. 3(e) and (f), V_{oc} and *FF* behaved similarly. Both of them dropped relatively quicker when t_{Si} became smaller than 20 μm. In comparison with the reduction of t_{Si} by 96.9%, the degradations were much smaller, only 25.9% and 30.1% for V_{oc} and *FF*, respectively. The increasing series resistance (R_s) and decreasing shunt resistance (R_{sh}) were the main reasons behind the decreasing *FF* as t_{Si} was reduced (Table 1). Because of the combined effects of J_{sc}, V_{oc}, and *FF*, the PCE (η) first dropped slightly by only 11.8% from 10.81% at t_{Si} = 200 μm to 9.53% at t_{Si} = 49.4 μm and then dropped a little bit dramatically to 6.61% and 4.24% at t_{Si} = 14.8 and 6.8 μm, respectively (Fig. 3(g) and Table 1). Alternatively, 88.2% of the initial PCE was maintained when 24.7% of the wafer was used; while when t_{Si} became less than 10% (or even 3.4%) of the initial thickness, 61.2% and 39.2% of the initial PCE were still achieved for the cells with t_{Si} = 14.8 and 6.8 μm, respectively. Overall, the degradation rate of η was much smaller than the reduction rate of t_{Si}. Greatly reducing the c-Si wafer thickness would not affect the power conversion performance too much, and further indicated a cost-effective way to optimize the c-Si solar cells.

EQE spectra of two representative c-Si solar cells with t_{Si} = 49.4 and 200 μm were plotted in Fig. 4. It was found that EQE of the thin cell rivalled that of the thick cell in the wavelength range of around 600–860 nm, but was lower both in the short range below about 600 nm and in the long range beyond about 860 nm. Specifically, in the short wavelength range, most incident photons were absorbed in the top part of the wafer for both thick and thin solar cells. They had similar absorption behaviors. However, due to the rough surface and the reduced minority carrier lifetime (Fig. 2(e) and (f)), the photogenerated

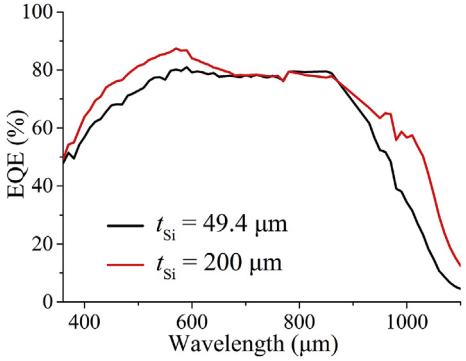

Fig. 4. Measured EQE spectra of two representative solar cells with t_{Si} = 49.4 (red) and 200 (black) μm, respectively.

carriers in the thin etched solar cell were more prone to be recombined before being selectively collected by the front Ag/MoO_x contact, resulting in a lower EQE in this range. As the wavelength increased, photons went deeper into and even reached the bottom Al/LiF_x contact, which played increasing roles in both positively enhancing light trapping via its high reflectivity and negatively reducing the photocarriers due to the lower carrier lifetime (Fig. 2(f)). The balance made a relatively flat EQE spectrum in the middle wavelength range for the thin solar cell. In the 3 times thicker cell, the generated carriers had to transport a much longer way to be collected with a much larger probability to be recombined in the bulk. Thus, the EQE decreased and eventually became comparable to that of the thin solar cell in this range. Beyond about 860 nm, the photons could not be well trapped in the thin solar cell, whose absorption became much smaller. Despite the greatly reduced carrier transportation length, the EQE still could not rival that of the thick solar cell. Fortunately, the whole EQE spectrum of the thin cell was not far below that of the thick cell (Fig. 4). Thus, J_{sc} of the thin cell was not reduced much as the wafer thickness decreased from 200 μm to 49.4 μm (Fig. 3 and Table 1).

3.3. Passivating and carrier-selective effects of the evaporated MoO_x and LiF_x films

As demonstrated in Fig. 2(f), the evaporated MoO_x enhanced minority carrier lifetime. In order to further investigate that effect, the interfaces of MoO_x on both original and etched c-Si surfaces were inspected by a TEM and shown in Fig. 5(a) and (b), respectively. Surprisingly, an apparent interlayer was observed with high contrast for both cases and the interlayer thicknesses were both about 3.6 nm (over 1 nm thicker than that reported in Ref. [46]). EDS profiles of Mo, O, and Si along the depths from MoO_x into c-Si were measured and they showed almost the same distributions for both the original and etched cases. The profiles of one case were plotted in Fig. 5(c). Mo and O dominated the top MoO_x layer while Si was the main element in the bottom c-Si wafer as expected. Between them, there was a small region, corresponding to the interlayer observed in Fig. 5(a) and (b), where Mo and O dropped quickly while Si rose quickly. Mo, O, and Si were all present in the interlayer, well consistent with the results observed by the time of flight secondary ion-mass spectroscopy in Ref. [46]. Therefore, it could be reasonably inferred that part of the O went from the MoO_x layer to the c-Si wafer, chemically oxidizing and passivating the c-Si surface. The fact that the O intensity was relatively lower in the middle of the MoO_x layer than that near the interlayer (Fig. 5(c)) further confirmed the movement of the O element and its deficiency in the MoO_x layer. Such defects were clearly observed by the XPS spectrum near the valence band region of the MoO_x film (Fig. 5(d)). The oxide interlayer passivated the dangling bonds at the c-Si surface and this was the main reason behind the increased lifetime after the deposition of the MoO_x film for both the original and etched c-Si samples (Fig. 2(f)).

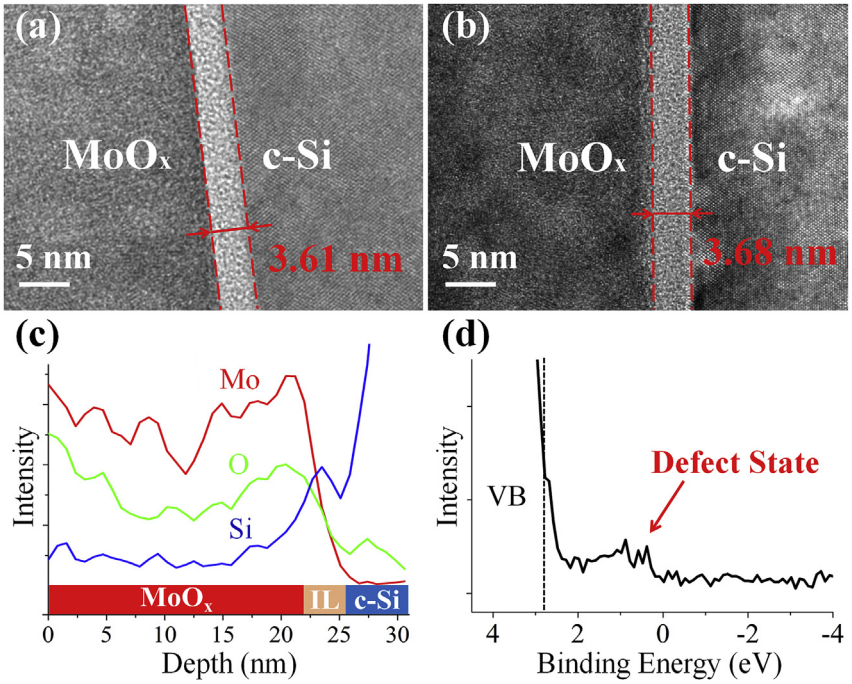

Fig. 5. TEM images of the interlayers between MoO_x and (a) the original c-Si sample and (b) the etched c-Si sample. (c) EDS element profiles along the depth from the top MoO_x layer to the c-Si wafer. (d) XPS spectrum near the valence band (VB) region of the evaporated MoO_x film.

Unlike MoO_x, LiF_x could not chemically passivate the surface dangling bonds [21]. No interlayer was observed by the TEM inspection at the interface between LiF_x and c-Si (Fig. S3, Supporting Information). It was also shown that the ~2-nm thick LiF_x film could coat on the rough c-Si surface uniformly and conformally. It was thick enough to completely separate Al and c-Si. The contamination of Al atoms could be avoided. Even without the Al electrode, the pure LiF_x coating still reduced the minority carrier lifetime for both the original and etched c-Si wafers (Fig. 2(f)). This implied that additional defects were introduced by the LiF_x thin film, probably serving as recombination centers for minority carriers. The defects were mainly Li atoms reduced from Li^+ ions, as inspected by XPS (to be demonstrated below). Fortunately, transportation of electrons was not much affected by the defective LiF_x layer (to be explained in detail below).

Compared with the original c-Si sample, the etched c-Si sample had a rougher surface morphology (Fig. 2(e)) and a smaller lifetime (Fig. 2(f)), but V_{oc} and *FF* of the thin c-Si solar cells did not drop too much (Fig. 3 and Table 1). Since the chemical passivation effect of the oxide interlayer was always very weak, there must be some other effects, such as field-effect passivation and carrier-selective conduction [47].

Systematic XPS inspection of the evaporated MoO_x and LiF_x films were conducted. The Mo 3d and Li 1s core level spectra were plotted in Fig. 5(a) and (b), respectively. The Mo 3d core level was split into the $3d_{5/2}$ and $3d_{3/2}$ doublet centered at 232.8 and 236.0 eV, respectively (Fig. 6(a)). The deconvolution of the spectrum showed that the doublet corresponded to the Mo^{6+} valence state (green curve), in good agreement with the previously-reported results in Ref. [24]. The Mo^{5+} valence state was also identified at the 3.1 eV lower binding energy (pink curve). It indicated again that oxygen vacancies existed in the MoO_x film (where $x < 3$), leading to defect states at the valence band region (Fig. 5(d)). These oxygen vacancies increased the conductivity of the evaporated MoO_x. From the deconvolution of the spectrum shown in Fig. 6(b), both Li^+ (green curve) and Li (pink curve) were detected, indicating some of the Li^+ ions were reduced with $x < 1$. Due to the slightly reduced cation oxidation states, the evaporated LiF_x film was more conductive. The existence of Li atoms confirmed our inference about the reason for the reduced carrier lifetime of the samples with LiF_x coatings (Fig. 2(f)).

According to the valence band maxima and their deviations from the core levels of MoO_x, LiF_x, and c-Si, as well as the core level differences between c-Si and MoO_x or LiF_x, valence band offsets at the MoO_x/c-Si and LiF_x/c-Si interfaces could be easily predicted, i.e., $\Delta E_v = 1.7$ eV and 5.25 eV, respectively. Together with the bandgap values of MoO_x (3.2 eV [29]), LiF_x (> 10 eV [21]), and c-Si (1.1 eV), the relative positions of the energy levels were plotted roughly in Fig. S6, Supporting Information. Details could be found in Section S4, Supporting Information. Subsequently, based on the rough band alignment, we proposed a reasonable band diagram for the c-Si heterojunction solar cell based on the dopant-free MoO_x and LiF_x contacts, which was plotted in Fig. 7 and discussed below.

The large workfunction difference between MoO_x (5.4 eV) and the n-type c-Si (4.2 eV) [44] drove Fermi level equilibration and consequently at the equilibrium at the MoO_x/c-Si interface, both the conduction band and the valence band near this interface were bent up (Fig. 7). The former provided a barrier for photogenerated electrons (with the conduction band offset of $\Delta E_c = 0.4$ eV shown in Fig. S6, Supporting Information), while the latter introduced a surface p^+-type inversion layer appropriate for hole transfer. In this case, with different carrier concentrations, their recombination was further inhibited in addition to the chemical passivating effect of the oxide interlayer. The band bending led to a built-in potential (V_{bi}). Assuming a strong inversion was formed and V_{bi} was close to 0.7 V, the remaining energy difference of about 0.5 eV must be allocated by negative dipoles for compensating the large workfunction difference (i.e., 1.2 eV). Such dipoles were probably induced by the oxygen defect states in the evaporated MoO_x film, where the transferred holes recombined with the negative defect states. Due to the band bending, the large valence band difference of $\Delta E_v = 2.15$ eV for the separated MoO_x and c-Si decreased to $\Delta E_v = 1.7$ eV when they were brought in touch, as shown in Fig. S6 in Section S4, Supporting Information. Such a reduction of ΔE_v was favorable for the hole transportation, though 1.7 eV was still very large. Fortunately, the insulating oxide interlayer was sufficiently thin (Fig. 5(a) and (b)), and the photogenerated holes were able to transfer

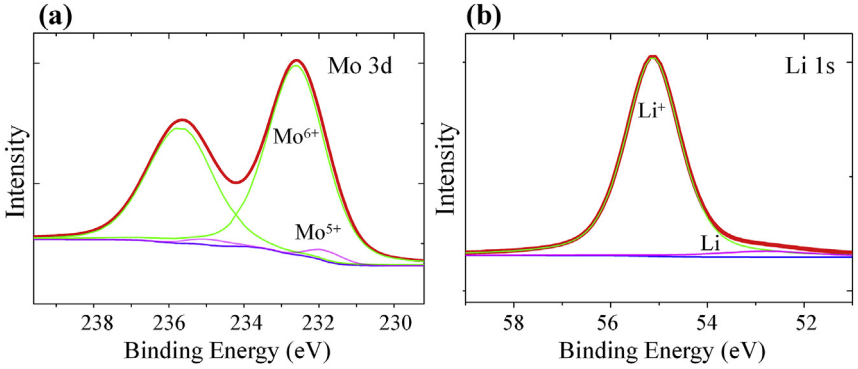

Fig. 6. XPS spectra of (a) the Mo 3d core level of the evaporated MoO_x film and (b) the Li 1s core level of the evaporated LiF_x film. The fitted components are also shown in color (Mo^{6+} and Li^+: green; Mo^{5+} and Li: pink).

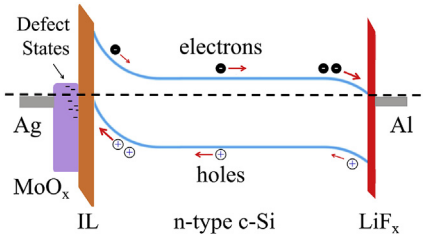

Fig. 7. Band diagram for the c-Si heterojunction solar cell based on dopant-free MoO_x and LiF_x contacts.

across it and be extracted to the Ag electrode with the assistance of the negative defect states. As a result of the above effects, the contact resistivity of the Ag and MoO_x films with the n-type c-Si wafer was adequately small, i.e., about 2.12 Ω·cm^2, which was measured based on a transfer length method. In contrast, without the MoO_x layer, an apparent rectification effect appeared during the contact resistivity measurement, meaning rather poor hole transportation. With a twice thicker Ag film on the MoO_x layer, a comparable contact resistivity of about 2.22 Ω·cm^2 was achieved, indicating that the ~100-nm Ag film was thick enough for conduction. Details were described in Section S5, Supporting Information.

With a thin layer of LiF_x inserted between the Al electrode and the n-type c-Si wafer, the workfunction of the Al electrode (~4.3 eV) could be greatly reduced to about 2.8 eV [21,35]. Such low workfunction made both the conduction band and the valence band near the interface bent down (Fig. 7). The former introduced a surface n^+-type electron accumulation layer appropriate for electron transfer, while the latter formed a barrier for photogenerated holes (with a large ΔE_v = 5.25 eV shown in Fig. S6, Supporting Information). With the accumulation layer, the Fermi level pinning effect was weakened. Though there was a large unfavorable ΔE_c > 3.65 eV at the interface (Fig. S6, Supporting Information), the photogenerated electrons could still be easily extracted through the ultrathin LiF_x layer (~2 nm thick), and good Ohmic contact was obtained. The improvement of electron extraction with the LiF_x insertion layer was also observed in e.g., organic solar cells [48]. Here in this work, the contact resistivity of the Al and LiF_x films with the n-type c-Si wafer was about 215 mΩ·cm^2, which was measured using the Cox-Strack approach (details was described in Section S5, Supporting Information). Without the LiF_x layer, the minority carrier lifetime was reduced (even became too low to measure for the etched sample; Section S6, Supporting Information) and rectified current-voltage curves were measured, indicating the negative effect of Fermi level pinning. This however reinforced the importance of the ~2-nm thick LiF_x film between the Al electrode and the n-type c-Si wafer in electron-selective conduction.

From the above analysis, it could be seen that for the MoO_x layer, both the chemical passivation effect induced by the oxide interlayer, and the field-effect passivation induced by the band bending worked for the efficient passivated hole-selective conduction; while for the LiF_x layer, only field-effect passivation played a main role for the efficient passivated electron-selective conduction. Due to these properties, the c-Si solar cells could maintain high performances (especially V_{oc} and *FF*), even when the wafer thickness was reduced (Fig. 3 and Table 1). Equally important roles were played by MoO_x, as the hole-selective contact, and LiF_x, as the electron-selective contact, in carrier separation and collection. Note that no additional passivation layers were deposited between MoO_x or LiF_x and c-Si in this work. This inevitably affected adversely the overall performances of c-Si solar cells. But fortunately, the superiority of our thin c-Si solar cells can still be well demonstrated, which is the main focus of this work. On the other hand, no additional passivation allowed us to observe the oxide interlayer between MoO_x and c-Si. The inherent passivation effects of MoO_x and LiF_x were clearly analyzed.

4. Conclusion

In conclusion, c-Si thin, flexible wafers with thicknesses of 6.8, 14.8 and 49.4 μm have been fabricated through KOH etching. On these thin wafers, thin c-Si heterojunction solar cells have been demonstrated experimentally based on the dopant-free carrier-selective contacts (substoichiometric MoO_x and LiF_x) for the first time. In comparison with the solar cell fabricated on the original 200-μm thick c-Si wafer, the much smaller degradation in power conversion performance results from the passivating and carrier-selective effects of the evaporated MoO_x and LiF_x films. An oxide interlayer was created at the MoO_x/c-Si interface, where the surface dangling bonds could be passivated and the minority carrier lifetime was improved. The band bending near the MoO_x/c-Si interface and the Al/LiF_x/c-Si interface introduced field-effect passivation and carrier-selective effects, which played an important role in maintaining V_{oc} and *FF*. There is still large room for performance improvement of our fabricated thin c-Si heterojunction solar cells. For example, light trapping schemes can be introduced to further improve the sunlight absorption in thin c-Si wafers and consequently J_{sc}, while more effective passivation layers, such as intrinsic a-Si:H, can be employed to further increase V_{oc} and *FF*. Our c-Si solar cells have been fabricated on thin c-Si wafers with low-temperature processes and without any additional doping, providing a promising cost-effective way to produce thin and flexible c-Si solar cells.

Acknowledgments

The authors would thank Le Kang and Mengzhu Hu for their preliminary efforts to this work, as well as Dr. Julian Evans for helpful discussions. This work was supported by the National Natural Science Foundation of China (Nos. 91833303 and 61775195), the National Key Research and Development Program of China (No. 2017YFA0205700),

and the Fundamental Research Funds for the Central Universities (No. 2019FZA5002).

Appendix A. Supplementary data

Supplementary data to this article can be found online at https://doi.org/10.1016/j.nanoen.2019.103930.

References

[1] J. Zhao, A. Wang, M.A. Green, 24· 5% Efficiency silicon PERT cells on MCZ substrates and 24· 7% efficiency PERL cells on FZ substrates, Prog. Photovolt. Res. Appl. 7 (1999) 471–474.

[2] M.A. Green, The path to 25% silicon solar cell efficiency: history of silicon cell evolution, Prog. Photovolt. Res. Appl. 17 (2009) 183–189.

[3] K. Masuko, M. Shigematsu, T. Hashiguchi, D. Fujishima, M. Kai, N. Yoshimura, T. Yamaguchi, Y. Ichihashi, T. Mishima, N. Matsubara, Achievement of more than 25% conversion efficiency with crystalline silicon heterojunction solar cell, IEEE J. Photovolt. 4 (2014) 1433–1435.

[4] K. Yoshikawa, H. Kawasaki, W. Yoshida, T. Irie, K. Konishi, K. Nakano, T. Uto, D. Adachi, M. Kanematsu, H. Uzu, Silicon heterojunction solar cell with interdigitated back contacts for a photoconversion efficiency over 26%, Nature Energy 2 (2017) 17032.

[5] M.A. Green, Y. Hishikawa, E.D. Dunlop, D.H. Levi, J. Hohl-Ebinger, A.W.Y. Ho-Baillie, Solar cell efficiency tables (version 52), Prog. Photovolt. Res. Appl. 26 (2018) 427–436.

[6] W. Shockley, H.J. Queisser, Detailed balance limit of efficiency of p-n junction solar cells, J. Appl. Phys. 32 (1961) 510–519.

[7] A. Richter, S.W. Glunz, F. Werner, J. Schmidt, A. Cuevas, Improved quantitative description of Auger recombination in crystalline silicon, Phys. Rev. B 86 (2012) 165202.

[8] D. Yan, A. Cuevas, Empirical determination of the energy band gap narrowing in p + silicon heavily doped with boron, J. Appl. Phys. 116 (2014) 194505.

[9] J. Oh, H.-C. Yuan, H.M. Branz, An 18.2%-efficient black-silicon solar cell achieved through control of carrier recombination in nanostructures, Nat. Nanotechnol. 7 (2012) 743.

[10] S.C. Baker-Finch, K.R. McIntosh, D. Yan, K.C. Fong, T.C. Kho, Near-infrared free carrier absorption in heavily doped silicon, J. Appl. Phys. 116 (2014) 063106.

[11] A. Descoeudres, C. Allebé, N. Badel, L. Barraud, J. Champliaud, G. Christmann, F. Debrot, A. Faes, J. Geissbühler, J. Horzel, Low-temperature processes for passivation and metallization of high-efficiency crystalline silicon solar cells, Sol. Energy 175 (2018) 54–59.

[12] C. Battaglia, A. Cuevas, S. De Wolf, High-efficiency crystalline silicon solar cells: status and perspectives, Energy Environ. Sci. 9 (2016) 1552–1576.

[13] A. Cuevas, T. Allen, J. Bullock, Y. Wan, X. Zhang, "Skin care for healthy silicon solar cells," 2015 IEEE 42nd Photovoltaic Specialist Conference (PVSC).

[14] T.G. Allen, J. Bullock, P. Zheng, B. Vaughan, M. Barr, Y. Wan, C. Samundsett, D. Walter, A. Javey, A. Cuevas, Calcium contacts to n-type crystalline silicon solar cells, Prog. Photovolt. Res. Appl. 25 (2017) 636–644.

[15] Y. Wan, C. Samundsett, D. Yan, T. Allen, J. Peng, J. Cui, X. Zhang, J. Bullock, A. Cuevas, A magnesium/amorphous silicon passivating contact for n-type crystalline silicon solar cells, Appl. Phys. Lett. 109 (2016) 113901.

[16] B. Liao, B. Hoex, A.G. Aberle, D. Chi, C.S. Bhatia, Excellent c-Si surface passivation by low-temperature atomic layer deposited titanium oxide, Appl. Phys. Lett. 104 (2014) 253903.

[17] G. Sahasrabudhe, S.M. Rupich, J. Jhaveri, A.H. Berg, K.A. Nagamatsu, G. Man, Y.J. Chabal, A. Kahn, S. Wagner, J.C. Sturm, Low-temperature synthesis of a TiO2/Si heterojunction, J. Am. Chem. Soc. 137 (2015) 14842–14845.

[18] X. Yang, P. Zheng, Q. Bi, K. Weber, Silicon heterojunction solar cells with electron selective TiOx contact, Sol. Energy Mater. Sol. Cells 150 (2016) 32–38.

[19] Y. Wan, C. Samundsett, J. Bullock, M. Hettick, T. Allen, D. Yan, J. Peng, Y. Wu, J. Cui, A. Javey, Conductive and stable magnesium oxide electron-selective contacts for efficient silicon solar cells, Adv. Energy Mater. 7 (2017) 1601863.

[20] Z. Yang, P. Gao, J. Sheng, H. Tong, C. Quan, X. Yang, K.W.A. Chee, B. Yan, Y. Zeng, J. Ye, Principles of dopant-free electron-selective contacts based on tunnel oxide/low work-function metal stacks and their applications in heterojunction solar cells, Nano Energy 46 (2018) 133–140.

[21] J. Bullock, P. Zheng, Q. Jeangros, M. Tosun, M. Hettick, C.M. Sutter-Fella, Y. Wan, T. Allen, D. Yan, D. Macdonald, Lithium fluoride based electron contacts for high efficiency n-type crystalline silicon solar cells, Adv. Energy Mater. 6 (2016) 1600241.

[22] Y. Wan, C. Samundsett, J. Bullock, T. Allen, M. Hettick, D. Yan, P. Zheng, X. Zhang, J. Cui, J. McKeon, Magnesium fluoride electron-selective contacts for crystalline silicon solar cells, ACS Appl. Mater. Interfaces 8 (2016) 14671–14677.

[23] T.G. Allen, J. Bullock, Q. Jeangros, C. Samundsett, Y. Wan, J. Cui, A. Hessler-Wyser, S. De Wolf, A. Javey, A. Cuevas, A low resistance calcium/reduced titania passivated contact for high efficiency crystalline silicon solar cells, Adv. Energy Mater. 7 (2017) 1602606.

[24] C. Battaglia, X. Yin, M. Zheng, I.D. Sharp, T. Chen, S. McDonnell, A. Azcatl, C. Carraro, B. Ma, R. Maboudian, Hole selective MoOx contact for silicon solar cells, Nano Lett. 14 (2014) 967–971.

[25] C. Battaglia, S.M. De Nicolas, S. De Wolf, X. Yin, M. Zheng, C. Ballif, A. Javey, Silicon heterojunction solar cell with passivated hole selective MoOx contact, Appl. Phys. Lett. 104 (2014) 113902.

[26] J. Bullock, A. Cuevas, T. Allen, C. Battaglia, Molybdenum oxide MoOx: a versatile hole contact for silicon solar cells, Appl. Phys. Lett. 105 (2014) 232109.

[27] J. Geissbühler, J. Werner, S. Martin de Nicolas, L. Barraud, A. Hessler-Wyser, M. Despeisse, S. Nicolay, A. Tomasi, B. Niesen, S. De Wolf, 22.5% efficient silicon heterojunction solar cell with molybdenum oxide hole collector, Appl. Phys. Lett. 107 (2015) 081601.

[28] M. Bivour, J. Temmler, H. Steinkemper, M. Hermle, Molybdenum and tungsten oxide: high work function wide band gap contact materials for hole selective contacts of silicon solar cells, Sol. Energy Mater. Sol. Cells 142 (2015) 34–41.

[29] L.G. Gerling, S. Mahato, A. Morales-Vilches, G. Masmitja, P. Ortega, C. Voz, R. Alcubilla, J. Puigdollers, Transition metal oxides as hole-selective contacts in silicon heterojunctions solar cells, Sol. Energy Mater. Sol. Cells 145 (2016) 109–115.

[30] D. Xu, X. Yu, D. Gao, C. Li, M. Zhong, H. Zhu, S. Yuan, Z. Lin, D. Yang, Self-generation of a quasi p–n junction for high efficiency chemical-doping-free graphene/silicon solar cells using a transition metal oxide interlayer, J. Mater. Chem. 4 (2016) 10558–10565.

[31] J. Meyer, S. Hamwi, M. Kröger, W. Kowalsky, T. Riedl, A. Kahn, Transition metal oxides for organic electronics: energetics, device physics and applications, Adv. Mater. 24 (2012) 5408–5427.

[32] Y. Liu, Z.-G. Zhang, Z. Xia, J. Zhang, Y. Liu, F. Liang, Y. Li, T. Song, X. Yu, S.-T. Lee, High performance nanostructured silicon–organic quasi p–n junction solar cells via low-temperature deposited hole and electron selective layer, ACS Nano 10 (2015) 704–712.

[33] Z. Yang, P. Gao, J. He, W. Chen, W.-Y. Yin, Y. Zeng, W. Guo, J. Ye, Y. Cui, Tuning of the contact properties for high-efficiency Si/PEDOT:PSS heterojunction solar cells, ACS Energy Lett 2 (2017) 556–562.

[34] Q. Liu, R. Ishikawa, S. Funada, T. Ohki, K. Ueno, H. Shirai, Highly efficient solution-processed poly (3, 4-ethylenedio-xythiophene): poly (styrenesulfonate)/Crystalline–Silicon heterojunction solar cells with improved light-induced stability, Adv. Energy Mater. 5 (2015) 1500744.

[35] J. Bullock, M. Hettick, J. Geissbühler, A.J. Ong, T. Allen, C.M. Sutter-Fella, T. Chen, H. Ota, E.W. Schaler, S. De Wolf, Efficient silicon solar cells with dopant-free asymmetric heterocontacts, Nature Energy 1 (2016) 15031.

[36] H.-D. Um, N. Kim, K. Lee, I. Hwang, J.H. Seo, K. Seo, Dopant-free all-back-contact Si nanohole solar cells using MoO x and LiF films, Nano Lett. 16 (2016) 981–987.

[37] S.Y. Herasimenka, W.J. Dauksher, S.G. Bowden, > 750 mV open circuit voltage measured on 50 μ m thick silicon heterojunction solar cell, Appl. Phys. Lett. 103 (2013) 053511.

[38] S. Wang, B.D. Weil, Y. Li, K.X. Wang, E. Garnett, S. Fan, Y. Cui, Large-area free-standing ultrathin single-crystal silicon as processable materials, Nano Lett. 13 (2013) 4393–4398.

[39] J.H. Petermann, D. Zielke, J. Schmidt, F. Haase, E.G. Rojas, R. Brendel, 19%-efficient and 43 μm-thick crystalline Si solar cell from layer transfer using porous silicon, Prog. Photovolt. Res. Appl. 20 (2012) 1–5.

[40] M.S. Branham, W.C. Hsu, S. Yerci, J. Loomis, S.V. Boriskina, B.R. Hoard, S.E. Han, G. Chen, 15.7% efficient 10-μm-thick crystalline silicon solar cells using periodic nanostructures, Adv. Mater. 27 (2015) 2182–2188.

[41] S. Jeong, M.D. McGehee, Y. Cui, All-back-contact ultra-thin silicon nanocone solar cells with 13.7% power conversion efficiency, Nat. Commun. 4 (2013) 2950.

[42] J. He, P. Gao, M. Liao, X. Yang, Z. Ying, S. Zhou, J. Ye, Y. Cui, Realization of 13.6% efficiency on 20 μm thick Si/organic hybrid heterojunction solar cells via advanced nanotexturing and surface recombination suppression, ACS Nano 9 (2015) 6522–6531.

[43] T. He, J. Yao, Photochromism of molybdenum oxide, J. Photochem. Photobiol. C Photochem. Rev. 4 (2003) 125–143.

[44] P. Kou, L. Yang, K. Chi, S. He, Large-area and uniform transparent electrodes fabricated by polymethylmethacrylate-assisted spin-coating of silver nanowires on rigid and flexible substrates, Opt. Mater. Express 5 (2015) 2347–2358.

[45] P. Kou, L. Yang, C. Chang, S. He, Improved flexible transparent conductive electrodes based on silver nanowire networks by a simple sunlight illumination approach, Sci. Rep. 7 (2017) 42052.

[46] L.G. Gerling, C. Voz, R. Alcubilla, J. Puigdollers, Origin of passivation in hole-selective transition metal oxides for crystalline silicon heterojunction solar cells, J. Mater. Res. 32 (2017) 260–268.

[47] Z. Yang, H. Lin, K.W.A. Chee, P. Gao, J. Ye, The role of front-surface charges in interdigitated back contact silicon heterojunction solar cells, Nano Energy 61 (2019) 221–227.

[48] C.J. Brabec, S.E. Shaheen, C. Winder, N.S. Sariciftci, P. Denk, Effect of LiF/metal electrodes on the performance of plastic solar cells, Appl. Phys. Lett. 80 (2002) 1288–1290.

Hao Dai received the B. Eng. degree from Zhejiang University, Hangzhou, China, in 2016, where he continues his research toward the Master's degree. His current research interests include crystalline silicon solar cells, particularly those with dopant-free carrier-selective contacts.

Liu Yang received the Ph.D. degree from Zhejiang University, Hangzhou, China, in 2009. Between 2009 and 2010, she was with the University of Michigan-Shanghai Jiao Tong University Joint Institute, Shanghai, China, as a research assistant. Since 2011, she has been with the College of Optical Science and Engineering, Zhejiang University, as a postdoctoral fellow, a research associate professor, and currently an associate professor. Her current research interests include photovoltaic solar cells and micro-/nano-photonics.

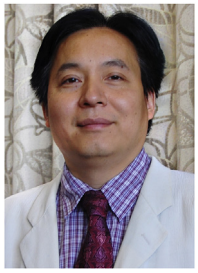

Sailing He received the Licentiate of Technology and the Ph.D. degree from the Royal Institute of Technology (KTH), Stockholm, Sweden, in 1991 and 1992, respectively. Since 1992, he has worked at KTH as an assistant professor, an associate professor, and a full professor. He also serves as the director for JORCEP (a Sino-Swedish joint research center of photonics) and a professor at Zhejiang University (China). His current research interests include subwavelength photonics and their applications. He has authored/co-authored about 600 papers in refereed international journals. He is a Fellow of IEEE, OSA, SPIE, and the Electromagnetics Academy.